LASER & PHOTONICS REVIEWS
www.lpr-journal.org

A Universal Strategy to Enhance Circularly Polarized Luminescence Brightness in Chiral Perovskites

Zhengwei Yang, Haolin Lu, Yu Zhang, Baipeng Yin, Hong Wang, Sehrish Gull, Wei Qin, Yongsheng Chen, Jiannian Yao, Chuang Zhang, and Guankui Long**

Chiral perovskites are considered as promising candidates for circularly polarized luminescence (CPL) light source, by attracting the broader scientific community for their applications in chiral optoelectronics and spintronics. However, it is still a great challenge to achieve both substantial photoluminescence asymmetry (g_{CPL}) and high photoluminescence quantum yield (PLQY) simultaneously for high CPL brightness due to the limitations associated with magnetic transition dipole moments. Herein, this problem is overcome and achieve both large g_{CPL} of 1.6×10^{-2} and PLQY of 56% in chiral perovskite through the magnetic element doping strategy. The substitution of Pb^{2+} ion with smaller magnetic Mn^{2+} ions shrinks the crystal lattice around $[MnBr_6]^{4-}$ octahedra, amplifying the asymmetric distortion surrounding the Mn^{2+} ions. Moreover, the transition associated with Mn^{2+} ions can harvest the photoexcitation energy in chiral perovskites, and its spin-flipping characteristics enable highly efficient CPL from the *d–d* transition on Mn^{2+} energy levels. Furthermore, this magnetic element doping strategy is proven to be a universal tactic for enhancing CPL brightness as confirmed in a series of 1D- or 2D-chiral perovskites with various chiral ligands or halogens. The findings provide an in-depth understanding of the structure-property relationship in chiral perovskites toward chiral optoelectronic and spintronic applications.

1. Introduction

Circularly polarized luminescence (CPL) refers to the preferential emission of left- or right-handed circularly polarized light[1] stemming from the chiral excited states of luminescent materials,[2,3] and it has garnered significant attention due to its potential applications in 3D displays, optical information processing and opto-spintronics.[4–9] An ideal CPL emitter requires high CPL brightness (B_{CPL}, as shown in Equation (1)),[10,11] i.e., large absorption efficiency, large luminescence dissymmetry (g_{CPL}) and high photoluminescence quantum yield (PLQY),[12] which describe utilization efficiency of excitation light, the degree of polarization and overall light intensity of CPL output, respectively.

$$B_{CPL} = \xi_{abs} \times PLQY \times \frac{|g_{CPL}|}{2} \quad (1)$$

In principle, g_{CPL} is proportional to the projection of magnetic transition

Z. Yang, Y. Zhang, B. Yin, H. Wang, J. Yao, C. Zhang
Key Laboratory of Photochemistry
Beijing National Laboratory for Molecular Sciences
Institute of Chemistry
Chinese Academy of Sciences
Beijing 100190, China
E-mail: zhangc@iccas.ac.cn

Z. Yang, Y. Zhang, H. Wang
University of Chinese Academy of Sciences
Beijing 100049, China

H. Lu, S. Gull, G. Long
Tianjin Key Lab for Rare Earth Materials and Applications
School of Materials Science and Engineering
National Institute for Advanced Materials
Nankai University
Tianjin 300350, China
E-mail: longgk09@nankai.edu.cn

W. Qin
School of Physics
State Key Laboratory of Crystal Materials
Shandong University
Jinan 250100, China

Y. Chen
State Key Laboratory and Institute of Elemento-Organic Chemistry
The Centre of Nanoscale Science and Technology
College of Chemistry
Nankai University
Tianjin 300071, China

J. Yao
Institute of Molecular Engineering Plus
Fuzhou University
Fuzhou 350108, China

The ORCID identification number(s) for the author(s) of this article can be found under https://doi.org/10.1002/lpor.202400040

DOI: 10.1002/lpor.202400040

dipole moment (m) on electric transition dipole moment (μ), but is inversely proportional to μ itself (Equation (2)).[13,14]

$$g_{CPL} = \frac{4\mu \cdot m \cdot \cos\theta}{\mu^2 + m^2} \approx \frac{4m \cdot \cos\theta}{\mu} \quad (2)$$

However, achieving a high PLQY in luminescent materials usually requires a large μ,[15] which brings the difficulty in simultaneously increasing both g_{CPL} and PLQY.[14] Several strategies have been proposed to address this issue, for instance, twisted π system is introduced to reduce the angle between m and μ and thus increase the projection of m;[16–18] spin-flipping of the d–d or f–f transition in transition metal and lanthanide complexes is utilized to enlarge m for enhanced CPL performance.[19,20] This spin-flipping of the d–d or f–f transition is proven to be the most efficient and straightforward strategies to increase m, and g_{CPL} of 1.4 was achieved in Cs[Eu((+)-hfbc)$_4$].[21] In this work, we are planning to employ this strategy to increase m, thus the g_{CPL} of chiral perovskites.

Chiral perovskites are regarded as an emerging class of circularly polarized luminescent hybrid materials[22–28] that are composed of organic chiral cations and inorganic metal-halide layers. They are expected to combine the advantages of both organic and inorganic components in optimizing their CPL brightness.[29–35] Especially, chiral cations can induce the symmetry-breaking distortion of the inorganic frameworks,[36–38] leading to the chirality transfer in hybrid perovskites that influences the radiative recombination of excited states located within the inorganic layers.[39] In addition, a variety of metal ions have been successfully incorporated into the inorganic frameworks, and could serve as luminescent centers involving ns^2 transition[40] or d–d/f–f transition[41,42] in hybrid perovskites. Very recently, Mn-doped hybrid perovskites were designed and synthesized, which exhibit relatively high PLQY due to the energy transfer from the perovskite host to the Mn^{2+} dopant.[42–46] Nevertheless, the spin-flipping of d–d transition of Mn^{2+} and its impact on the CPL performance of chiral perovskites have not yet been explored.

In this study, we have systematically investigated the influence of magnetic element doping on the magnetic transition dipole moment, photoluminescence asymmetry, photoluminescence quantum yield, and thus the CPL brightness of chiral perovskite. The manganese-doped chiral perovskite (S/R-2-NEA$_2$Pb$_{1-x}$Mn$_x$Br$_4$, 2-NEA: 2-naphthylethylamine) exhibits large g_{CPL} of 1.60 $\times 10^{-2}$, together with high PLQY of 56%, which is remarkably improved compared with that of undoped S/R-NEA$_2$PbBr$_4$ ($g_{CPL} < 2 \times 10^{-3}$, PLQY $\approx$ 1%). Most importantly, the Mn-doped chiral perovskite exhibits the highest CPL brightness among all the reported chiral perovskite films. The substitution of Pb^{2+} ions with smaller Mn^{2+} ions causes the shrinkage of crystal lattice around $[MnBr_6]^{4-}$ octahedra, which consequently amplifies the asymmetric distortion surrounding Mn^{2+} ions. Meanwhile, the energy transfer from free excitons (FEs) to Mn^{2+} ions leads to the enhanced PL emission from doped perovskites, which is attributed to the d–d transition of Mn^{2+} as demonstrated by the temperature-dependent PL spectroscopy and PL dynamics. The electron paramagnetic resonance (EPR) and magneto-PL (MPL) measurements further elucidate the spin-flipping characteristics of Mn^{2+} d–d transitions, which, together with the increased chiral distortions in the doped perovskites, contribute to the enhancement of CPL performance. The enhancement in CPL brightness by Mn^{2+} doping is also achieved in other 1D- or 2D-chiral perovskites with various ligands or halogens, further confirming the universality of our magnetic element doping strategy toward enhanced circularly polarized luminescence brightness in chiral perovskites. Thus, these Mn-doped chiral perovskites hold great potential for the development of CPL emitters in advanced display technologies and spin-optoelectronic applications.

2. Results and Discussion

As shown in **Scheme 1**, we have designed a chiral 2D perovskite using 2-naphthylethylamine (2-NEA) with large steric hindrance as the chiral spacers to prevent the collapse of the inorganic $[PbBr_6]^{4-}$ structures. The anionic layers of corner-sharing $[PbBr_6]^{4-}$ octahedra are separated by the bilayers of 2-NEA$^+$ cations. The substitution of Pb^{2+} ions with smaller Mn^{2+} ions causes a shrinkage of the crystal lattice around $[MnBr_6]^{4-}$ octahedron, which leads to an increased mean penetration depth of NH_3^+ approaching the inorganic framework.[37] This, in turn, enhances the asymmetric NH···Br hydrogen bonding interactions between the NH_3^+ group of organic cations and the inorganic framework,[36–38] which would enhance the asymmetric distortion surrounding the Mn^{2+} ions (Figure S1, Supporting Information). Density functional theory (DFT) calculations (Figure S2, Supporting Information) reveal that in both undoped and Mn-doped perovskites, the valence band maximum (VBM) is primarily composed of Br 4p orbitals, while the conduction band minimum (CBM) is mainly constituted by Pb 6p orbitals. Upon photoexcitation, FEs are generated near the band-edge of perovskite, and then relax to a lower energy level in the transiently distorted lattice and form self-trapped excitons (STEs). In the case of Mn-doped perovskite, two energy levels ($^6A_{1g}$, $^4T_{1g}$) associated with Mn^{2+} ions are introduced within the bandgap, and energy transfer occurs from FEs to Mn^{2+} ions, exhibiting magnified circular-polarized radiative decay through spin-flipping on the Mn^{2+} energy levels.

High-quality single crystals of S-2-NEA$_2$PbBr$_4$ were grown using the slow-cooling method, and they crystallized in the $P2_1$ *Sohncke* space group as confirmed by single crystal X-ray diffraction (SC-XRD) (Table S1, Supporting Information). S-2-NEA$_2$Pb$_{1-x}$Mn$_x$Br$_4$ powder was synthesized (x is the Mn/(Pb + Mn) molar ratio in precursor solutions, and x = 0–0.6) through a hydrobromic acid-assisted solution mixing strategy,[44] and images of S-2-NEA$_2$Pb$_{1-x}$Mn$_x$Br$_4$ with the molar ratio from 0 to 0.3 are shown in **Figure 1a**. Notably, the undoped sample exhibits very weak PL, while the Mn-doped samples display strong orange PL under UV excitation (Figure 1a). Compared with the simulated XRD based on single crystal (Table S2 and Figure S3, Supporting Information), the experimental diffraction peak at 4.34° of S-2-NEA$_2$PbBr$_4$ polycrystalline films should be assigned to the (*001*) crystal plane, suggesting that the orientation of the layered structure is highly parallel to the substrate (Figure 1b). The characteristic peak of the (*001*) plane shifts slightly to higher diffraction angle and then remains unchanged as x increases from 0 to 0.3 for Mn^{2+} doping. The corresponding d-spacing of the (*001*) plane, calculated from the XRD patterns, is reduced from 20.36 Å for S-2-NEA$_2$PbBr$_4$ to 19.69 Å for S-NEA$_2$Pb$_{0.8}$Mn$_{0.2}$Br$_4$, which

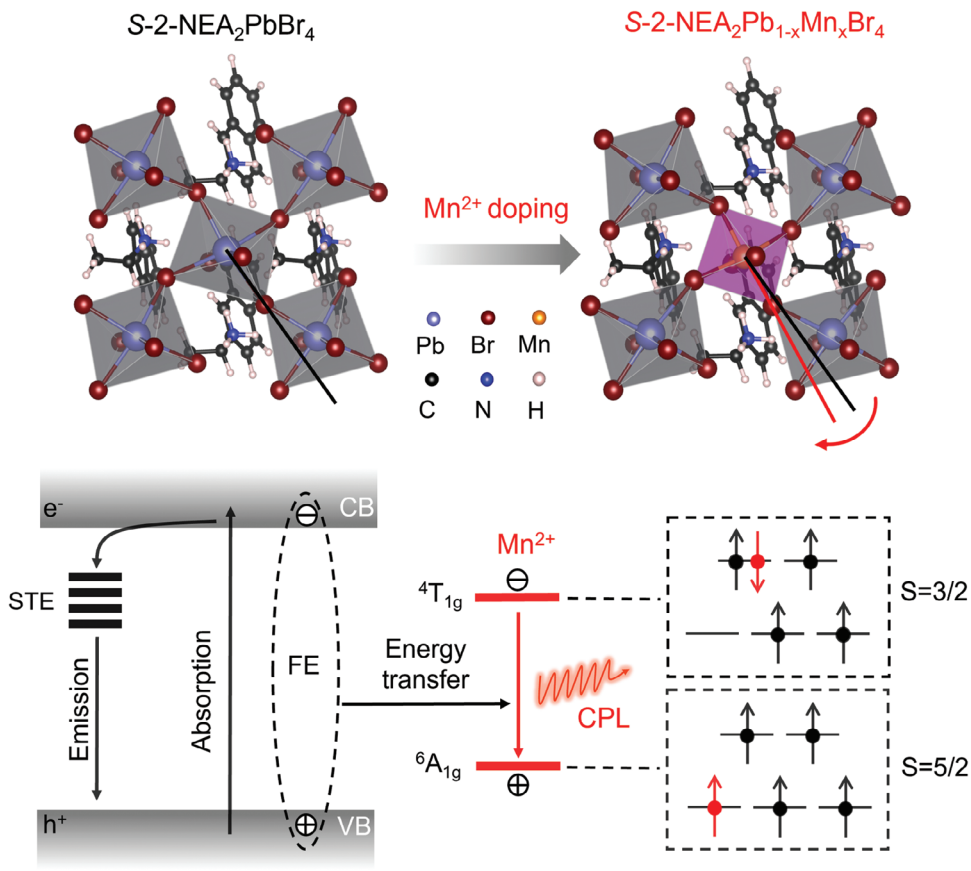

Scheme 1. Schematic illustration for the structural distortion upon Mn^{2+} doping (top) and the excited state processes involving energy transfer in chiral perovskites (bottom).

further confirms the lattice shrinkage upon Mn^{2+} doping. When the molar ratio is equal to 0.3, an additional diffraction peak emerges at 5.24° in the XRD patterns, which should be attributed to the formation of NEA_2MnBr_4 phase.[42]

To illustrate the distribution of Mn^{2+} ions in *S*-$NEA_2Pb_{0.8}Mn_{0.2}Br_4$, scanning electron microscopy (SEM) and energy dispersive X-ray spectrometry (EDS) characterizations were performed on their microcrystals, as shown Figure 1c. The elemental mapping results demonstrated that Mn^{2+} ions are uniformly distributed in the microcrystal, and this uniformity was consistently preserved in the *S*-$NEA_2Pb_{0.8}Mn_{0.2}Br_4$ films (Figure S4, Supporting Information).[45] Furthermore, X-ray photoelectron spectroscopy (XPS) measurements were adopted to characterize the chemical composition and covalent bonding in *S*-$NEA_2Pb_{0.8}Mn_{0.2}Br_4$ films,[42] as shown in Figure 1d. Two distinct peaks at 641.8 eV and 647.8 eV, corresponding to the Mn $2p_{3/2}$and Mn $2p_{1/2}$ electron energy levels, are exclusively detected in Mn-doped perovskite, further confirming the presence of Mn^{2+} ions in the crystal structure. Additionally, two peaks at 138.8 and 143.6 eV, corresponding to Pb $4f_{7/2}$ and Pb $4f_{5/2}$ electron energy levels, are shifted to higher binding energies by 0.3 eV after Mn^{2+} doping. This shift is ascribed to the shrinkage associated with the $[PbBr_6]^{4-}$ octahedra and the consequent strengthening of Pb—Br bond upon the incorporation of smaller Mn^{2+} ions.[47] According to the XPS element depth profiling (Table S3, Supporting Information), the content of Mn^{2+} ions in *S*-$NEA_2Pb_{0.8}Mn_{0.2}Br_4$ is estimated to be 7.5%.

Figure 2a,b shows the absorption and circular dichroism (CD) spectra of *S*/*R*-$NEA_2Pb_{0.8}Mn_{0.2}Br_4$ films along with their corresponding *S*/*R*-NEA_2PbBr_4 counterparts. The absorption spectra are dominated by the band-to-band transitions, and the excitonic absorption (peak at 388 nm) near the band edge is clearly observed. The band-to-band transitions are primarily governed by the transitions from Br 4p orbitals to Pb 6p orbitals, as supported by DFT calculations (Figure S2, Supporting Information). Upon the partial substitution of Pb^{2+} ions with Mn^{2+} ions, the transition probabilities for these band-to-band transitions decrease, resulting in a reduction of absorbance intensity. The band edge absorbance (*Urbach* tail) slightly increases for Mn-doped perovskites, which results from the distortions induced by the smaller Mn^{2+} ion substitution.[48] Furthermore, this structural distortion leads to a slight increase in the bandgap,[39] from 3.20 eV for *S*-NEA_2PbBr_4 to 3.27 eV for *S*-$NEA_2Pb_{0.8}Mn_{0.2}Br_4$, as determined from the Tauc plot (Figure S5, Supporting Information). CD spectra show a typical signal of bisignate Cotton effects[36] with a zero crossing point at the exciton absorption peak at 388 nm, while CD signals of the corresponding chiral cations do not expand 300 nm (Figure S6, Supporting Information). This distinction implies the chirality is successfully transferred from organic cations to inorganic sublattices,[37] and the

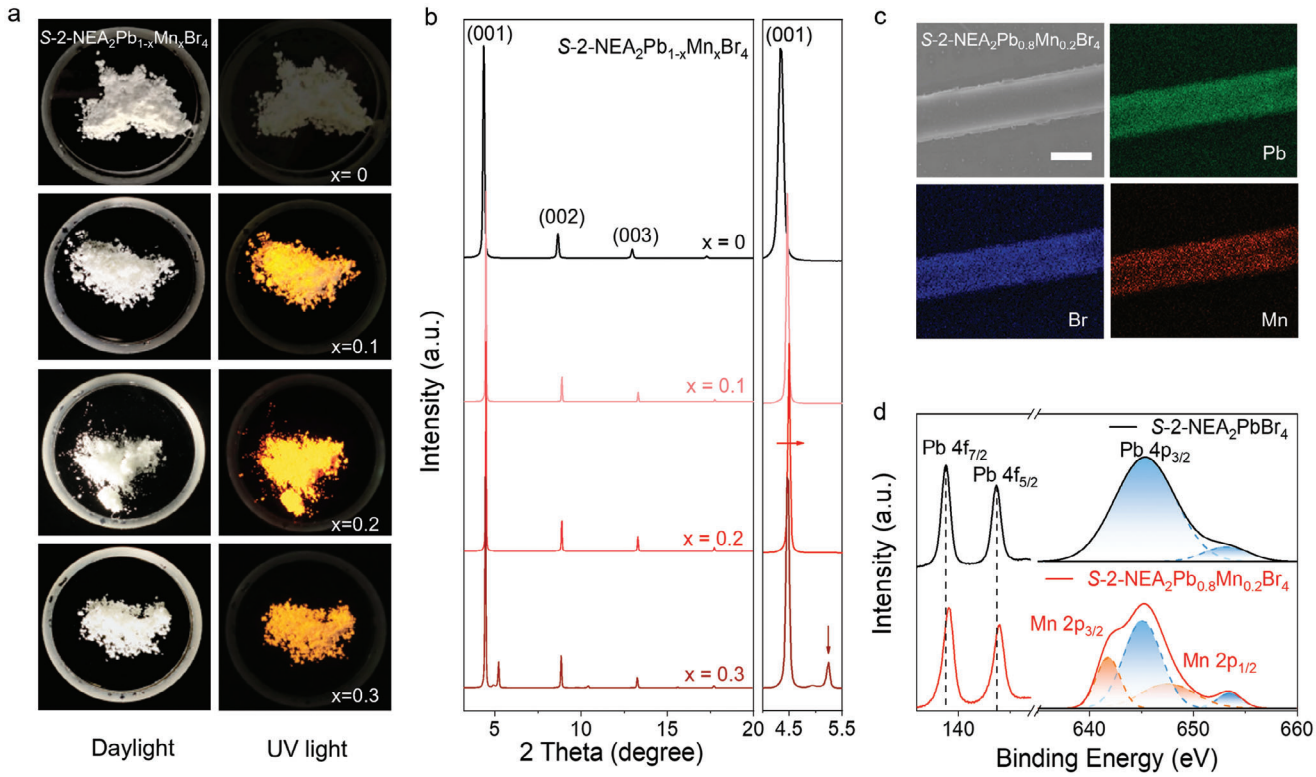

Figure 1. a) Photographs of *S*-2-NEA$_2$Pb$_{1-x}$Mn$_x$Br$_4$ (x is the Mn/(Pb + Mn) molar ratio, and x = 0, 0.1, 0.2, and 0.3) under daylight and UV light. b) XRD patterns of *S*-2-NEA$_2$Pb$_{1-x}$Mn$_x$Br$_4$ films, and magnified XRD patterns including the (001) crystal plane are shown on the right. c) SEM image of *S*-2-NEA$_2$Pb$_{0.8}$Mn$_{0.2}$Br$_4$ and EDS elemental mapping of Pb, Br and Mn in the microcrystal. The scale bar is 5 μm. d) High-resolution XPS analysis of Pb and Mn in undoped (top) and doped (bottom) *S*-2-NEA$_2$PbBr$_4$ samples.

CD signals arise from chiral perovskites instead of the corresponding chiral cations. These derivative-type CD signals can be attributed to the excited state splitting,[36] which is preferentially excited either by left or right-handed circularly polarized light. The deconvolutions of CD are shown in Figure S7 (Supporting Information), and the corresponding intensity is smaller for the Mn-doped perovskite, consistent with the absorption spectra. Additionally, opposite mirror-like CD signals are observed for *S*/*R* enantiomers due to their opposite chirality.

As shown in Figure 2c,d, undoped chiral perovskite exhibits a weak broadband emission ranging from 500 to 800 nm, attributed to STEs,[39] while Mn-doped perovskites display a strong emission centred at 633 nm, originating from Mn^{2+} ions in octahedral coordination geometry.[49–51] The PL spectra consistently maintain the characteristic shape of Mn^{2+} emission, irrespective of the excitation wavelengths or power intensities (Figure S8, Supporting Information). The PL intensity exhibits a near-linear increase with the excitation power intensities and reach saturation at higher excitation intensities exceeding 1000 mW cm^{-2}, further indicating the presence of highly efficient luminescence centers, namely Mn^{2+} ions. These PL features further exclude the possibility of defect-assisted emission.[52] Remarkably, a significant enhancement in the CPL for Mn-doped perovskites is observed compared to undoped perovskites. This remarkable increase in CPL, in contrast to no obvious change in CD, further implies the enhanced chiral distortion surrounding the Mn^{2+} ions and the associated emission properties of Mn^{2+} ions. Specifically, the g_{CPL} reaches 1.60×10^{-2} for *S*-NEA$_2$Pb$_{0.8}$Mn$_{0.2}$Br$_4$ and -1.54×10^{-2} for *R*-NEA$_2$Pb$_{0.8}$Mn$_{0.2}$Br$_4$, whereas the g_{CPL} values are estimated to be below 2×10^{-3} for the undoped chiral perovskites. Mirror-symmetric CPL spectra are obtained for *S*/*R*-enantiomers, while the racemate shows no CPL signals (Figure S9, Supporting Information). These CPL results do not reverse upon films rotation or flipping (Figure S10, Supporting Information), and the CPL signals could be reproduced well. Thus, artifacts in our CPL measurement could be excluded. To further optimize the CPL performance, we measured the PLQY and corresponding g_{CPL} across a range of initial molar ratios (x) of *S*-NEA$_2$Pb$_{1-x}$Mn$_x$Br$_4$ from 0.1 to 0.6 in the precursor solutions (Figure 2e). Notably, the PLQY is dominantly increased upon Mn^{2+} doping, with a maximum PLQY of 56% achieved at a molar ratio of 0.2 (Figure S11, Supporting Information). Similarly, the g_{CPL} is also significantly enhanced compared with that of the undoped perovskite, reaching a maximum of 1.60×10^{-2} at the same molar ratio. Despite the gradual decrease in the g_{CPL} at higher Mn^{2+} ion concentrations, the g_{CPL} of the doped perovskite with a 0.6 molar ratio remains higher than that of the undoped perovskite. These trends in both PLQY and g_{CPL} are in accordance with the XRD results, where Mn^{2+} doping reaches saturation at a molar ratio of 0.2. Beyond this ratio, new peaks appear in the XRD patterns and the peak intensity increases with x (Figure S12, Supporting Information). A schematic representation of structural transformations with varying x from 0 to 0.6 is provided in Figure 2e. Notably, compared with *S*-NEA$_2$PbBr$_4$, the chiral

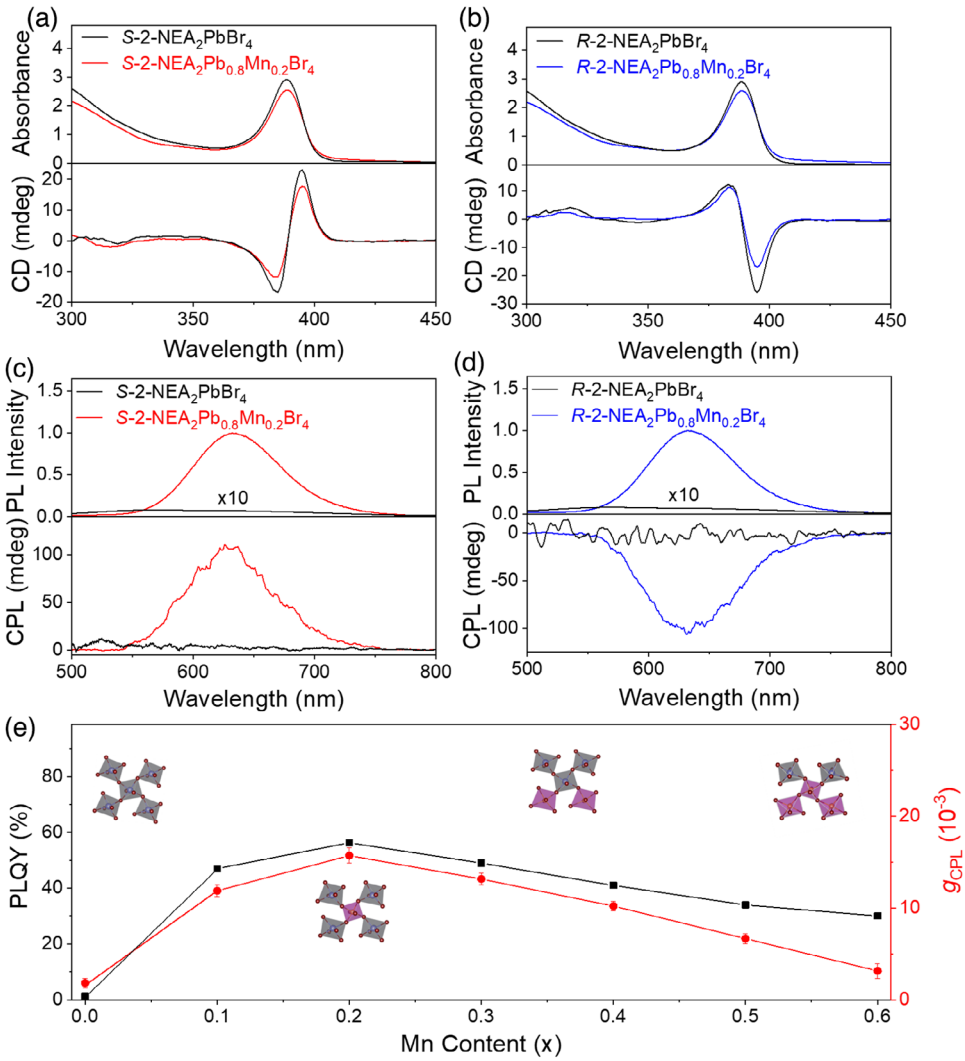

Figure 2. UV–vis absorption (top) and circular dichroism (CD) (bottom) spectra of a) *S*-NEA_2PbBr_4 (black line)/*S*-$NEA_2Pb_{0.8}Mn_{0.2}Br_4$ (red line) and b) *R*-NEA_2PbBr_4 (black line)/*R*-$NEA_2Pb_{0.8}Mn_{0.2}Br_4$ (blue line). Normalized PL (top) and CPL (bottom) spectra of c) *S*-NEA_2PbBr_4 (black line)/*S*-$NEA_2Pb_{0.8}Mn_{0.2}Br_4$ (red line) and d) *R*-NEA_2PbBr_4 (black line)/*R*-$NEA_2Pb_{0.8}Mn_{0.2}Br_4$ (blue line). e) PLQY and g_{CPL} of various *S*-$NEA_2Pb_{1-x}Mn_xBr_4$ (x = 0–0.6). Differences in g_{CPL} upon sample rotation are shown as error bars, and schematic inorganic frameworks for different x values are shown inside.

crystal structure becomes more distorted in *S*-$NEA_2Pb_{0.8}Mn_{0.2}Br_4$, which has a positive impact on CPL.[38,53] Subsequently, a new phase of nonluminous *S*-NEA_2MnBr_4 emerges and aggregates (Figure S13, Supporting Information), while Mn–Mn interaction becomes stronger due to shorter interatomic distances (Figure S14, Supporting Information), both of which have an adverse effect on the optical properties.[42]

The temperature-dependent PL and decay dynamics for *S*-2-$NEA_2Pb_{0.8}Mn_{0.2}Br_4$ and *S*-2-NEA_2PbBr_4 were further measured to gain further insights into the photophysical processes involved. As shown in **Figure 3**a, *S*-2-$NEA_2Pb_{0.8}Mn_{0.2}Br_4$ exhibits PL in the wavelength range from 550 to 750 nm across the temperature range from 6 K to 300 K, which is typical for Mn^{2+} ions in an octahedral O_h crystal field. The crystal field strength decreases with the increase of temperature due to thermal lattice expansion.[54] According to the Tanabe–Sugano diagram for Mn^{2+} ions,[54] a decrease in the field strength leads to a greater energy separation between the excited state $^4T_{1g}$ and the ground state $^6A_{1g}$, leading to a blueshift in PL peaks. In contrast, the PL peaks of STEs in the undoped perovskite exhibit a redshift with increasing temperature (Figure S15, Supporting Information), primarily due to electron–phonon coupling effects.[55,56] The distinctive behaviors observed in the temperature dependence of PL are indicative of energy transfer from FEs to Mn^{2+} ions in the Mn-doped perovskite, which is also demonstrated by the decreased exciton lifetime (Figure S16, Supporting Information). Additionally, the PL intensities exhibit temperature-dependent decrement, which follow the Arrhenius equation (Figure S17, Supporting Information). The activation energy (E_a) is found to be 192.7 meV for Mn^{2+} doped perovskite, which is significantly higher than that of undoped perovskite (54.1 meV). E_a represents the activation energy associated with the phonon-assisted

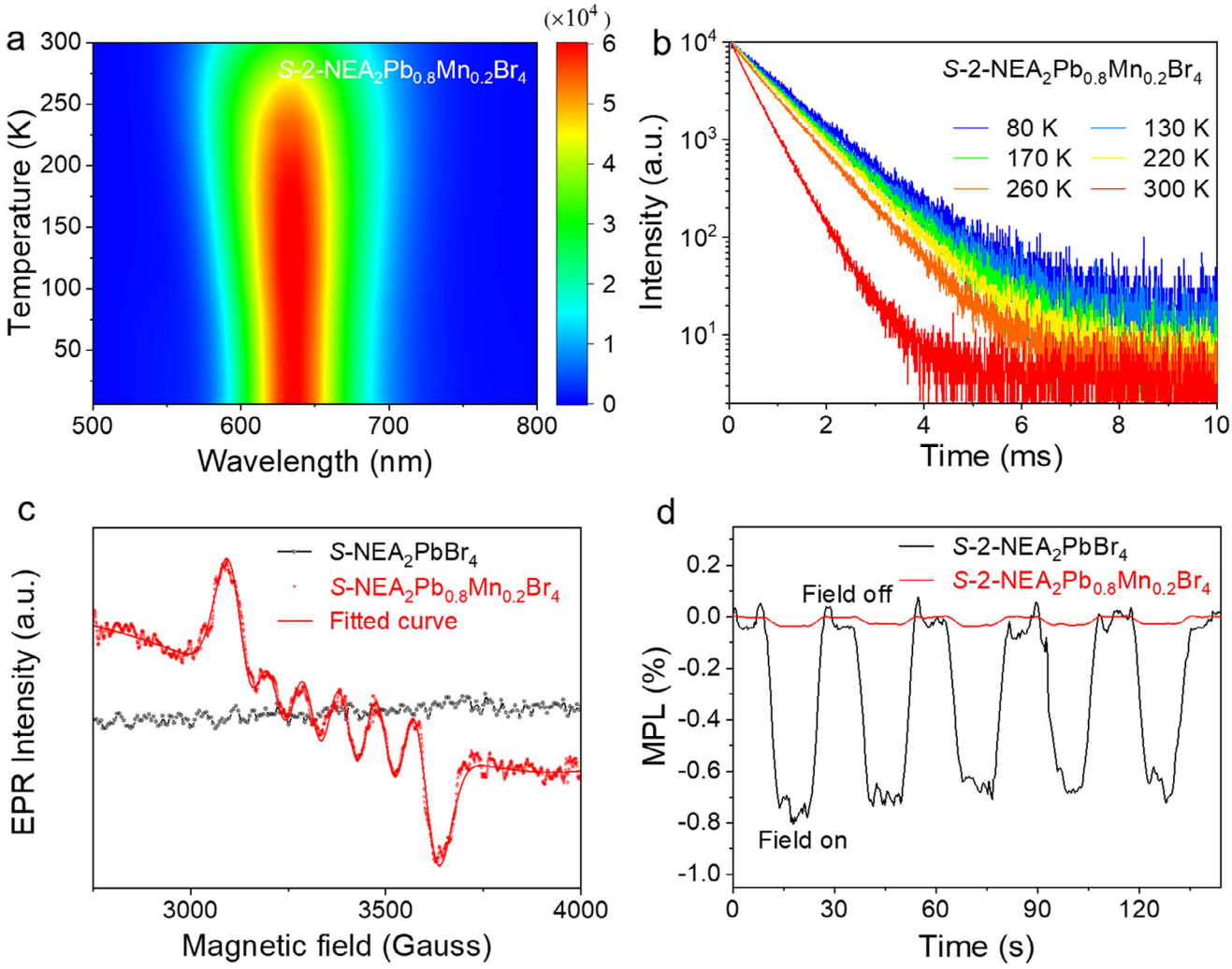

Figure 3. a) Temperature dependent steady-state PL between 6 and 300 K. b) Temperature dependent PL decay at 80, 130, 170, 220, 260, and 300 K. c) EPR spectra for *S*-NEA_2PbBr_4 (black) and *S*-2-$NEA_2Pb_{0.8}Mn_{0.2}Br_4$ (red). d) MPL of *S*-NEA_2PbBr_4 (black line) and *S*-2-$NEA_2Pb_{0.8}Mn_{0.2}Br_4$ (red line).

nonradiative recombination pathway, and a larger E_a can diminish the exciton dissociation, consequently enhancing radiative recombination and elevating PLQYs.[57] The phonon-assisted nonradiative recombination at higher temperatures also results in a decrease in the PL decay lifetime from 1.01 ms (at 80 K) to 0.17 ms (at 300 K), as shown in Figure 3b. Note that the PL lifetime of Mn-doped perovskites are in the millisecond range at all temperatures, which is a few orders of magnitude longer than those (nanoseconds) for undoped perovskites (Figure S15, Supporting Information). These prolonged PL lifetimes can be attributed to the spin-flipping characteristic of optical transitions associated with Mn^{2+} ions.[54]

We further conducted EPR and MPL measurements to elucidate the spin-flipping transitions in Mn-doped perovskites. As shown in Figure 3c, the EPR signals appear in the Mn-doped perovskite rather than that of undoped perovskite, which confirms the presence of net spins in the Mn^{2+} ions. The observed sextet hyperfine pattern could be well fitted and is attributed to the interaction between nuclear spin and S = 5/2 electron spin,[58] indicating that all five *d* orbitals of Mn^{2+} are occupied with five spin-parallel electrons in the ground state. This electron spin configuration of Mn^{2+} is further validated by spin-polarized DFT calculation. The spin-polarized partial density of states (PDOS) of the *d*-orbitals of Mn^{2+} in Mn-doped chiral perovskite is shown in Figure S18a (Supporting Information), which is occupied by only spin-up electrons. Then the integrated DOS (IDOS) of the net spins, which is defined as the difference between the IDOS of spin-up electrons and spin-down electrons is calculated. As shown in Figure S18b (Supporting Information), the IDOS of net spins is five at the Fermi level, indicating the *d* orbitals of Mn^{2+} is occupied by five spin-up electrons in Mn-doped chiral perovskite. The spin density of Mn^{2+} is further calculated and shown in Figure S18c (Supporting Information). This high-spin configuration implies the spin-flipping characteristics of *d*–*d* transition to a low-spin excited state, which may increase *m* for enhanced CPL.[19,59] The introduction of spin generated from transition metal will influence the optical properties in perovskites.[57,60–62] As shown in Figure 3d, we validate spintronic properties of Mn^{2+} on excited states by using the MPL measurements,[63] defined as: MPL(*B*) = [PL(*B*)-PL(0)]/PL(0), where PL(*B*) and PL(0) represent

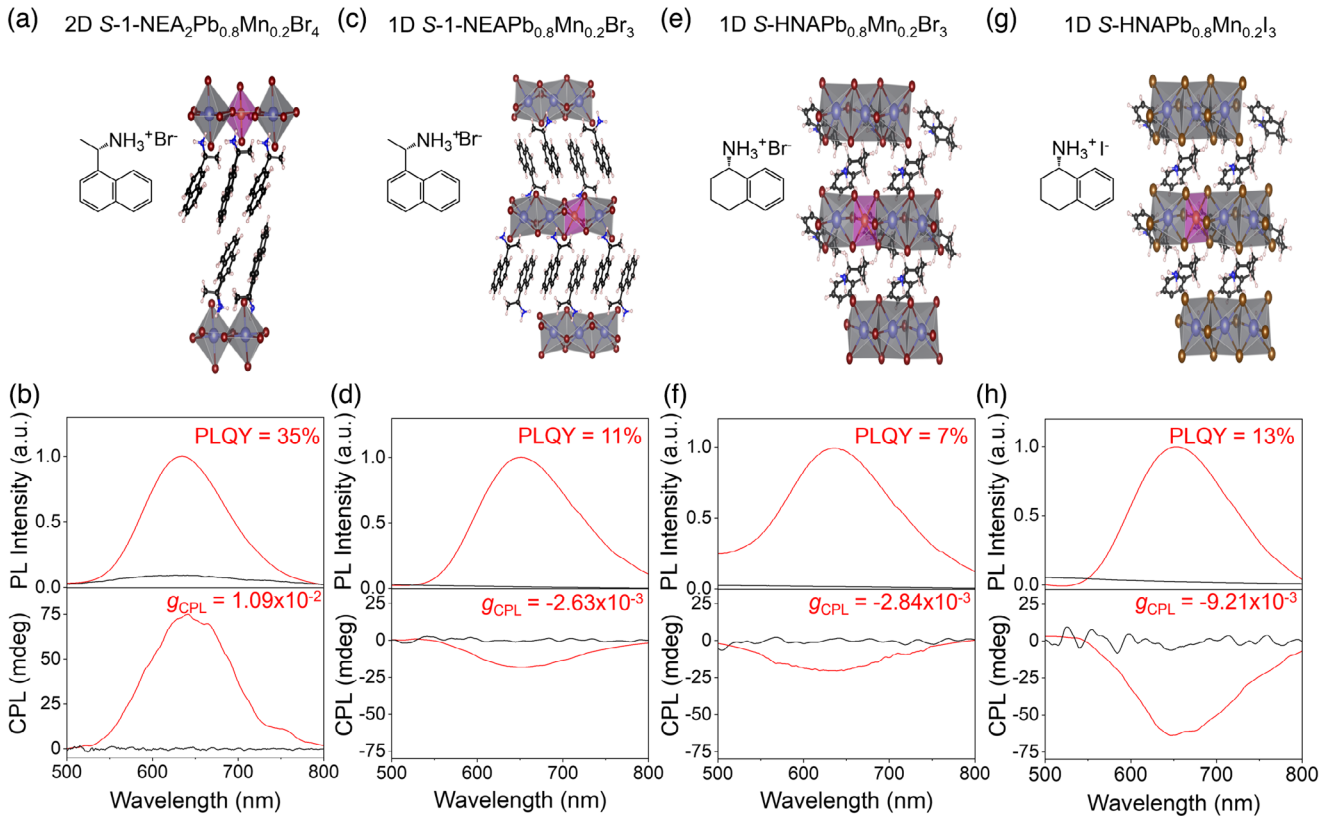

Figure 4. a) Schematic crystal structure of Mn-doped perovskite and corresponding molecular structure of chiral cations for a) *S*-1-$NEA_2Pb_{0.8}Mn_{0.2}Br_4$, c) *S*-1-$NEAPb_{0.8}Mn_{0.2}Br_3$, e) *S*-$HNAPb_{0.8}Mn_{0.2}Br_3$, and g) *S*-$HNAPb_{0.8}Mn_{0.2}I_3$. The PL (top) and CPL (bottom) of each doped perovskite (red lines) are shown below the crystal structure for b) *S*-1-NEA2$Pb_{0.8}Mn_{0.2}Br_4$, d) *S*-1-$NEAPb_{0.8}Mn_{0.2}Br_3$, f) *S*-1-$NEAPb_{0.8}Mn_{0.2}I_3$ and h) *S*-$HNAPb_{0.8}Mn_{0.2}I_3$. The black lines represent the results of the corresponding undoped perovskites.

PL intensities measured with and without a magnetic field B, respectively. When a magnetic field is applied, a decrement in the PL intensity is observed for undoped perovskite films, resulting in a negative MPL[64] of ≈0.7% due to changes in spin population of excitons for *S*-2-NEA_2PbBr_4.[62–65] In comparison, the MPL is substantially reduced to <0.05% for *S*-2-$NEA_2Pb_{0.8}Mn_{0.2}Br_4$, because fast energy transfer[46] occurs from FEs to Mn^{2+} ions and this spin-flipping *d*–*d* transition of Mn^{2+} is immune to external field owing to the enhanced exchange interaction. The above observations verify that the energy transfer from FEs to Mn^{2+} ions is predominant compared with the relaxation of FEs to STEs in Mn-doped chiral perovskites, leading to the improvements in both PLQY and g_{CPL} for CPL emission.

We then synthesized a series of chiral perovskites and systematically investigated their CPL brightness properties (PLQY and g_{CPL}) by replacing the chiral cations and/or halogens, as shown in **Figure 4**. Chiral 1-(1-naphthyl) ethylamine (1-NEA)[39] was introduced to obtain *S*-1-$NEA_2Pb_{0.8}Mn_{0.2}Br_4$ (Figure 4a) at a stoichiometric ratio of 2:1 for NEA/($MnBr_2$+$PbBr_2$), which exhibited a g_{CPL} of 1.09×10^{-2} and PLQY of 35% (Figure 4b). By adjusting the stoichiometric ratio to 1:1, we synthesized *S*-1-$NEAPb_{0.8}Mn_{0.2}Br_3$ (Figure 4c) and g_{CPL} of -2.63×10^{-3} and PLQY of 11% were obtained (Figure 4d). *S*-1-NEA_2PbBr_4 features 2D corner-sharing $[PbBr_6]^{4-}$ octahedral layers, while *S*-1-$NEAPbBr_3$ exhibits 1D face-sharing $[PbBr_6]^{4-}$octahedral chains, and the substitution of Pb^{2+} ions with Mn^{2+} ions within the 1D perovskite structure leads to a strong coupling between Mn 3*d* and Br 4*p* orbitals. This increases the crystal field strength of Mn^{2+} ions, resulting in a redshift of the PL peak from 635 nm for *S*-1- $NEA_2Pb_{0.8}Mn_{0.2}Br_4$ to 650 nm for *S*-1-$NEAPb_{0.8}Mn_{0.2}Br_3$. It is worth noting that the g_{CPL} exhibit opposite values between Mn-doped 2D *S*-1-NEA_2PbBr_4 and 1D *S*-1-$NEAPbBr_3$, which is probably induced by chiral structural differences.[66]

Furthermore, the 1D chiral perovskites *S*-$HNAPb_{0.8}Mn_{0.2}Br_3$ (Figure 4e) employing the *S*-1,2,3,4-tetrahydro-1-naphthalenamine (HNA) with a cyclo-alkyl group as chiral cation was synthesized, which exhibited g_{CPL} of 2.84×10^{-3} and PLQY of 7% (Figure 4f). By changing the halide ion from Br^- to I^- in the reactant, we also synthesized *S*-$HNAPb_{0.8}Mn_{0.2}I_3$ (Figure 4g) and g_{CPL} of -9.21×10^{-3} together with PLQY of 13% were achieved (Figure 4h). These two perovskites crystalized into the $P2_12_12_1$ and $P2_1$ *Sohncke* space group (Table S4, Supporting Information), respectively, with the arrangement of organic cations perpendicular to the inorganic $[PbBr_6]^{4-}$ octahedral chains. The more covalent nature of Mn-I bonds facilitates greater overlap between Mn 3*d* and I 5*p* orbitals,[67] resulting in a redshift in the PL peak from 638 nm for *S*-$HNAPb_{0.8}Mn_{0.2}Br_3$ to 655 nm for *S*-$HNAPb_{0.8}Mn_{0.2}I_3$ due to the increasement of the crystal field strength. Meanwhile, the large g_{CPL} observed in the I-based perovskite may be associated with the higher

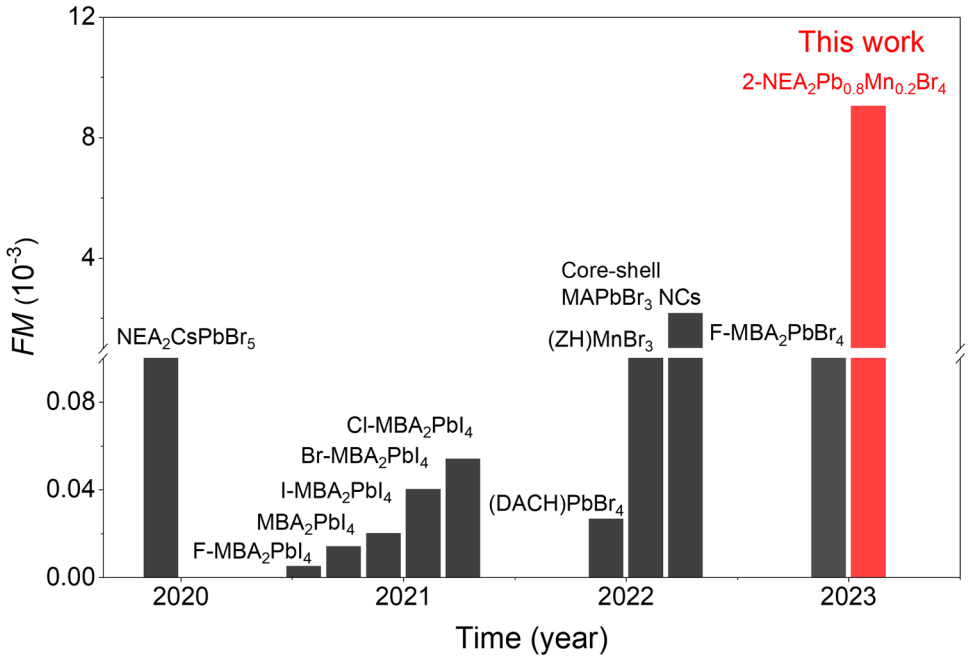

Figure 5. Comparison of the *FM* in literatures (black) and this work (red).

polarizability of iodine atoms, which promotes chiral distortion of the metal-halide octahedra through NH...I hydrogen bonds. Therefore, all these chiral perovskites with introducing the magnetic element display enhanced CPL brightness, with tenfold increment in PLQY and fivefold enhancement in g_{CPL}, compared with the corresponding undoped perovskite (black line in Figure 4). In addition, a figure of merit[11] (*FM*, as shown in Equation (3)) of these Mn-doped perovskite is adopted to assess the CPL brightness for comparison with those observed in other reported chiral perovskite films at room temperature.[12,13,38,68–70]

$$FM = PLQY \times |g_{CPL}| \quad (3)$$

All Mn-doped chiral perovskite films exhibit large *FM* values (Table S5, Supporting Information), with the highest value of 9.0×10^{-3} achieved in chiral 2-$NEA_2Pb_{0.8}Mn_{0.2}Br_4$ perovskite film (**Figure 5**).

3. Conclusion

In summary, we have successfully demonstrated a universal strategy for enhancing the CPL brightness by magnetic element doping in chiral perovskites. Notably, an improved CPL performance with g_{CPL} of 1.60×10^{-2} together with PLQY of 56% is achieved in chiral 2-$NEA_2Pb_{0.8}Mn_{0.2}Br_4$ perovskite film, compared with the undoped 2-NEA_2PbBr_4 ($g_{CPL} < 2 \times 10^{-3}$, PLQY ≈ 1%), and it is also the highest CPL brightness among all the reported chiral perovskite films. The Mn^{2+} ions were uniformly distributed in the lattice after partially replacing the Pb^{2+} ions, causing the structural shrinkage around $[MnBr_6]^{4-}$ octahedron and consequently amplifying the asymmetric distortion surrounding the Mn^{2+} ions. Meanwhile, the energy transfer from FEs to Mn^{2+} ions enhances the PL in the doped perovskites by exploiting the radiative decay of Mn^{2+} ions. The spin-flipping characteristics of the *d*–*d* transition of Mn^{2+}, which increases the magnetic transition dipole moment, together with the increased chiral distortions, contributed to the enhancement of g_{CPL}. Furthermore, this magnetic element doping strategy was proven to be a universal approach for enhancing the CPL brightness as confirmed in other 1D- or 2D-chiral perovskites with various ligands or halogens. These results present a promising strategy for improving CPL features and offer valuable insights for the design of effective CPL emitters suitable toward chiral optoelectronic and spintronic applications.

4. Experimental Section

Materials: Lead(II) bromide ($PbBr_2$, 98%), (*S*)-(-)-1-(1-naphthyl)ethylamine (*S*-1-NEA, 98%), (*R*)-(+)-1-(1-naphthyl)ethylamine (*R*-1-NEA, 98%), (*S*)-(+)-1,2,3,4-tetrahydro-1-naphthalenamine (*S*-HNA, 97%), (*R*)-(-)-1,2,3,4-tetrahydro-1-naphthalenamine (*R*-HNA, 97%), N,N-dimethylformamide (DMF, 99%), ethanol (EtOH, 99.5%), *n*-butanol (*n*-BuOH, 99%) and ethyl acetate (EtOAc, 99%) were purchased from Aladdin. (*S*)-(-)-1-(2-naphthyl)ethylamine (*S*-2-NEA, 98%) was purchased from Energy Chemical. (*R*)-(+)-1-(2-naphthyl)ethylamine (*R*-2-NEA, 99%), manganese(II) bromide ($MnBr_2$, 98%) and hydriodic acid (HI, 55–57 wt.% solution in H2O) were purchased from Innochem. Hydrobromic acid (HBr, 40 wt.% in H2O) was purchased from Macklin. All chemicals were used without further purification.

Synthesis: Synthesis of ammonium salts. For the synthesis of *S*-2-NEABr, 171 mg (1 mmol) *S*-2-NEA was dissolved in EtOH (3 mL) and then 40% wt.% aqueous HBr solution (1 mL) was added to EtOH solution with constant stirring to obtain a clear solution. After vigorous stirring for 3 h, the solution was fully evaporated to obtain *S*-2-NEABr solid precipitates. For the synthesis of *S*-1-NEABr, *S*-HNABr or *S*-HNAI salts, *S*-1-NEA (1 mmol) or *S*-HNA (1 mmol) was added into 40% wt.%

aqueous HBr solution (1.5 ml) and *S*-HNA (1 mmol) was added into 56 wt.% HI solution (1 mL), and vigorously stirred overnight. Then, the solution was filtered, and *S*-1-NEABr, *S*-HNABr or *S*-HNAI powders were washed with diethyl ether, and vacuum-70 °C for 2 h.

Synthesis of chiral perovskites. For the synthesis of *S*-2-NEA_2PbBr_4, 34.2 mg (0.2 mmol) *S*-2-NEA and 36.7 mg (0.1 mmol) $PbBr_2$ were dissolved in a mixture solvent of *n*-BuOH (1 mL) and 40% wt.% aqueous HBr solution (1 mL) at 363 K with constant stirring to obtain a clear solution. Single crystals were obtained using a slow cooling method from 363 K down to room temperature at a rate of 2 K h^{-1}. Other chiral perovskite single crystals were synthesized using a similar method. Specifically, for *S*-1-NEA_2PbBr_4: 50.4 mg (0.2 mmol) *S*-1-NEABr and 36.7 mg (0.1 mmol) $PbBr_2$ were dissolved in 40% *w/w* aqueous HBr solution (2 mL); for *S*-1-$NEAPbBr_3$: 25.2 mg (0.1 mmol) *S*-2-NEABr and 36.7 mg (0.1 mmol) $PbBr_2$ were dissolved in 40% *w/w* aqueous HBr solution (1.5 mL); for *S*-$HNAPbBr_3$: 22.8 mg (0.1 mmol) of *S*-HNA and 36.7 mg (0.1 mmol) of $PbBr_2$ were dissolved in 40% w/w aqueous HBr solution (3 mL); for *S*-$HNAPbI_3$: 27.5 mg (0.1 mmol) *S*-HNI and 46.1 mg (0.1 mmol) PbI_2 were dissolved in hydriodic acid, 56 wt.% solution in H2O (3 mL). Single crystals were obtained from solutions using a temperature-cooling method, washed with diethyl ether and dried in vacuum at 70 °C for 2 h. For the synthesis of *S*-2-$NEA_2Pb_{1-x}Mn_xBr_4$ (x = 0, 0.1, 0.2, 0.3), a hydrobromic acid-assisted solution mixing element was adopted. First, 1–x mmol $PbBr_2$ and x mmol $MnBr_2$ were dissolved in 1 ml of 40% w/w aqueous HBr, and 2 mmol *S*-2-NEA was dissolved in a solvent mixture of butanol (0.3 mL) and 40% w/w aqueous HBr solution (0.7 mL). Then, *S*-2-$NEA_2Pb_{1-x}Mn_xBr_4$ powders were precipitated by mixing these two solutions. After vigorous stirring for 3 h, the solution was concentrated to obtain the corresponding *S*-2-$NEA_2Pb_{1-x}Mn_xBr_4$ powders. In addition, *S*-2-$NEA_2Pb_{1-x}Mn_xBr_4$ microcrystals could be obtained, through slowly adding a solution containing metal ions to a solution containing amines. *S*-2-$NEA_2Pb_{1-x}Mn_xBr_4$ samples were filtered, washed with diethyl ether and dried in vacuum at 70 °C for 2 h. The *R* configuration were synthesized via the same preparation method as the *S* configuration.

Film Preparation: Quartz glasses were utilized as substrates, which were cleaned in an ultrasonic cleaner utilizing detergent, acetone, 2-propanol, ethanol, and deionized water in sequence for 15 min of each step. Next, the substrates were cleaned with an Ar–O_2 plasma cleaner for 10 min before they were used. First, 50.4 mg (0.2 mmol) *S*-2-NEABr and 36.7 mg (0.1 mmol) $PbBr_2$ were dissolved in 0.4 mL DMF and stirred at 363 K for 3 h to obtain 0.25 M transparent solution. 50 µl of the precursor solution was spin-coated on glass substrate at 500 rpm for 5 s and 3000 rpm for 30 s, and EtOAc (5 µl) was dropped onto this film at 10 s to form crystal nuclei. After that, this film was annealed at 398 K for 25 min. Other chiral perovskite films were prepared using a similar method. Specifically, the following reagents were employed for film preparation: for *S*-1-NEA_2PbBr_4 films: 50.4 mg (0.2 mmol) *S*-1-NEABr and 36.7 mg (0.1 mmol) $PbBr_2$; for *S*-1-$NEAPbBr_3$ films: 25.2 mg (0.1 mmol) *S*-2-NEABr and 36.7 mg (0.1 mmol) $PbBr_2$; for *S*-$HNAPbBr_3$ films: 22.8 mg (0.1 mmol) of *S*-HNA and 36.7 mg (0.1 mmol) of $PbBr_2$; and for *S*-$HNAPbI_3$ films: 27.5 mg (0.1 mmol) *S*-HNI and 46.1 mg (0.1 mmol) PbI_2. For Mn-doped perovskite films, the x molar ratio of $PbBr_2$ was replaced with the same amount of $MnBr_2$, and then the same preparation route was adopted to obtain *S*-2-$NEA_2Pb_{1-x}Mn_xBr_4$ films (x = 0.1, 0.2, 0.3, 0.4, 0.5 and 0.6) and other Mn-doped chiral perovskite films. Films with the *R* configuration was prepared via the same preparation method as the *S* configuration.

Characterization: Single crystal X-ray diffraction (SC-XRD) was performed on a Rigaku MM007HFSaturn724+ with Mo Kα radiation (0.71073 Å) at 170 K. Powder X-ray diffraction (PXRD) patterns were recorded using a PANalytical B.V. Empyrean diffractometer with Cu Kα (1.54 Å) radiation. The microscopic morphologies and elemental mapping were examined using a Hitachi SU8020 scanning electron microscope (SEM) with energy dispersive X-ray spectrometry (EDS). X-ray photoelectron spectroscopy (XPS) spectra were measured using an X-ray photoelectron spectrometer (ESCALAB250XI) at room temperature. The absorption spectra were measured using a UV–Vis spectrometer (Hitachi UH4150) at normal incidence, and the temperature-dependent PL spectra were measured from 6 K to 300 K using a homemade measurement system consisting of a cryostat (Montana Instruments Cryostation s50), a spectrometer (Princeston Instruments HRS300) and a charge-coupled device (CCD, Pixis 256). PL decay dynamics was obtained by an Edinburgh Instruments FLS 1000 from 80 to 300 K using its temperature control system. The absolute PL quantum yield was determined using Hamamatsu C11347 coupled with an integrating sphere. CD performances were measured using a commercial instrument JASCO J-1500. CPL performances were measured using a commercial instrument, JASCO CPL spectrophotometer (CPL-300) under 325 nm excitation, and both the excitation and emission slits are 3000 µm. Spectra are obtained at a scanning speed of 20 nm min^{-1}, and the data pitch is 1 nm. All films are accumulated 3 times to obtain the average results. Then, the films are tested by rotating them 90°, 180°, and 270° around the optical axis of the spectropolarimeter. Additionally, the samples are flipped to obtain the reliable CPL. The electron paramagnetic resonance (EPR) spectra were measured using a spectrometer (Bruker E500) at 100 K. MPL measurements were performed via a homemade measurement system consisting of a computer controlled electromagnet (Beijing Chaoruirenda Technology CR1), the excitation emission was 375 nm using a continuous wave laser (MDL-III-375), and the PL signals of the samples were extracted using a calibrated silicon photodiode which was transformed into electrical signals using a photomultiplier (Thorlab PDA200C) and finally collected using a digital multimeter (Keithley DMM6500).

The Vienna Ab-initio Simulation Package (VASP) software is used to accomplish the density functional theory (DFT) calculations. The projector augmented wave (PAW) method with the Perdew–Burke–Ernzerhof (PBE) functional are selected and the plane-wave cutoff energy is set to 500 eV. Gaussian smearing of 50 meV is used for all calculations. Geometric structures are relaxed without any limitation until the energies and total forces are converged to 10^{-5} eV and 0.001 eV $Å^{-1}$, respectively. Γ-centered Monkhorst–Pack mesh k points with k-spacing of 0.04π $Å^{-1}$ are employed for sampling the Brillouin zones for structural relaxations. Spin orbit coupling (SOC) is considered for calculations of free energies, densities of states. For the SOC band structure calculation, 20 points are inserted between each pair of high symmetry k points.

Supporting Information

Supporting Information is available from the Wiley Online Library or from the author.

Acknowledgements

This work was financially supported by the Ministry of Science and Technology of China (no. 2018YFA0704802 and 2020YFA0714603) and the National Natural Science Foundation of China (no. 22090021, 92256202 and 12261131500).

Conflict of Interest

The authors declare no conflict of interest.

Data Availability Statement

The data that support the findings of this study are available from the corresponding author upon reasonable request.

Keywords

chiral perovskites, chirality, circularly polarized luminescence, energy transfer, manganese dope

Received: January 8, 2024
Revised: March 4, 2024
Published online:

[1] Y. Sang, J. Han, T. Zhao, P. Duan, M. Liu, *Adv. Mater.* **2020**, *32*, 1900110.
[2] G. Long, C. Jiang, R. Sabatini, Z. Yang, M. Wei, L. N. Quan, Q. Liang, A. Rasmita, M. Askerka, G. Walters, X. Gong, J. Xing, X. Wen, R. Quintero-Bermudez, H. Yuan, G. Xing, X. R. Wang, D. Song, O. Voznyy, M. Zhang, S. Hoogland, W. Gao, Q. Xiong, E. H. Sargent, *Nat. Photon.* **2018**, *12*, 528.
[3] J. Crassous, M. J. Fuchter, D. E. Freedman, N. A. Kotov, J. Moon, M. C. Beard, S. Feldmann, *Nat. Rev. Mater.* **2023**, *8*, 365.
[4] J. L. Greenfield, J. Wade, J. R. Brandt, X. Shi, T. J. Penfold, M. J. Fuchter, *Chem. Sci.* **2021**, *12*, 8589.
[5] X. Liu, K. Wang, T. Zhang, H. Liu, A. Ren, S. Ren, P. Li, C. Zhang, J. Yao, Y. S. Zhao, *Adv. Mater.* **2023**, *35*, 2305260.
[6] G. Long, R. Sabatini, M. I. Saidaminov, G. Lakhwani, A. Rasmita, X. Liu, E. H. Sargent, W. Gao, *Nat. Rev. Mater.* **2020**, *5*, 423.
[7] M. Wang, Z. Yang, C. Zhang, *Adv. Opt. Mater.* **2021**, *9*, 2002236.
[8] J. Ni, C. Huang, L. M. Zhou, M. Gu, Q. Song, Y. Kivshar, C. W. Qiu, *Science* **2021**, *374*, eabj0039.
[9] S.-H. Yang, R. Naaman, Y. Paltiel, S. S. P. Parkin, *Nat. Rev. Phys.* **2021**, *3*, 328.
[10] L. Arrico, L. Di Bari, F. Zinna, *Chem. - Eur. J.* **2021**, *27*, 2920.
[11] L. Yao, G. Niu, J. Li, L. Gao, X. Luo, B. Xia, Y. Liu, P. Du, D. Li, C. Chen, Y. Zheng, Z. Xiao, J. Tang, *J. Phys. Chem. Lett.* **2020**, *11*, 1255.
[12] J. Chen, S. Zhang, X. Pan, R. Li, S. Ye, A. K. Cheetham, L. Mao, *Angew. Chem., Int. Ed.* **2022**, *61*, 202205906.
[13] D. Di Nuzzo, L. Cui, J. L. Greenfield, B. Zhao, R. H. Friend, S. C. J. Meskers, *ACS Nano* **2020**, *14*, 7610.
[14] Z. L. Gong, X. F. Zhu, Z. H. Zhou, S. W. Zhang, D. Yang, B. Zhao, Y. P. Zhang, J. P. Deng, Y. X. Cheng, Y. X. Zheng, S. Q. Zang, H. Kuang, P. F. Duan, M. J. Yuan, C. F. Chen, Y. S. Zhao, Y. W. Zhong, B. Z. Tang, M. H. Liu, *Sci. China Chem.* **2021**, *64*, 2060.
[15] L. Tao, H. Zhan, Y. Cheng, C. Qin, L. Wang, *J. Phys. Chem. Lett.* **2023**, *14*, 2317.
[16] Z. Qiu, C. W. Ju, L. Frederic, Y. Hu, D. Schollmeyer, G. Pieters, K. Mullen, A. Narita, *J. Am. Chem. Soc.* **2021**, *143*, 4661.
[17] T. He, M. Lin, H. Wang, Y. Zhang, H. Chen, C. L. Sun, Z. Sun, X. Y. Wang, H. L. Zhang, Y. Chen, G. Long, *Adv. Theory Simul.* **2024**, *7*, 23005.
[18] Y. Nakai, T. Mori, Y. Inoue, *J. Phys. Chem. A* **2012**, *116*, 7372.
[19] W. R. Kitzmann, K. Heinze, *Angew. Chem., Int. Ed.* **2023**, *62*, 202213207.
[20] B. Doistau, J. R. Jimenez, C. Piguet, *Front. Chem.* **2020**, *8*, 555.
[21] J. L. Lunkley, D. Shirotani, K. Yamanari, S. Kaizaki, G. Muller, *J. Am. Chem. Soc.* **2008**, *130*, 13814.
[22] L. Zhang, L. Mei, K. Wang, Y. Lv, S. Zhang, Y. Lian, X. Liu, Z. Ma, G. Xiao, Q. Liu, S. Zhai, S. Zhang, G. Liu, L. Yuan, B. Guo, Z. Chen, K. Wei, A. Liu, S. Yue, G. Niu, X. Pan, J. Sun, Y. Hua, W.-Q. Wu, D. Di, B. Zhao, J. Tian, Z. Wang, Y. Yang, L. Chu, et. al., *Nano-Micro Lett.* **2023**, *15*, 177.
[23] S. Jiang, N. A. Kotov, *Adv. Mater.* **2023**, *35*, 2108431.
[24] H. Wang, J. Li, H. Lu, S. Gull, T. Shao, Y. Zhang, T. He, Y. Chen, T. He, G. Long, *Angew. Chem., Int. Ed.* **2023**, *62*, e202309600.
[25] Y. Hu, F. Florio, Z. Chen, W. A. Phelan, M. A. Siegler, Z. Zhou, Y. Guo, R. Hawks, J. Jiang, J. Feng, L. Zhang, B. Wang, Y. Wang, D. Gall, E. F. Palermo, Z. Lu, X. Sun, T. M. Lu, H. Zhou, Y. Ren, E. Wertz, R. Sundararaman, J. Shi, *Sci. Adv.* **2020**, *6*, eaay4213.
[26] H. Lu, T. He, H. Wu, F. Qi, H. Wang, B. Sun, T. Shao, T. Qiao, H. L. Zhang, D. Sun, Y. Chen, Z. Tang, G. Long, *Adv. Funct. Mater.* **2023**, *33*, 2308862.
[27] X. Yang, X. Gao, Y.-X. Zheng, H. Kuang, C.-F. Chen, M. Liu, P. Duan, Z. Tang, *CCS Chem.* **2023**, *5*, 2760.
[28] A. Pietropaolo, A. Mattoni, G. Pica, M. Fortino, G. Schifino, G. Grancini, *Chem* **2022**, *8*, 1231.
[29] S. Liu, M. Kepenekian, S. Bodnar, S. Feldmann, M. W. Heindl, N. Fehn, J. Zerhoch, A. Shcherbakov, A. Pöthig, Y. Li, U. W. Paetzold, A. Kartouzian, I. D. Sharp, C. Katan, J. Even, F. Deschler, *Sci. Adv.* **2023**, *9*, eadh5083.
[30] Y. H. Kim, Y. Zhai, E. A. Gaulding, S. N. Habisreutinger, T. Moot, B. A. Rosales, H. Lu, A. Hazarika, R. Brunecky, L. M. Wheeler, J. J. Berry, M. C. Beard, J. M. Luther, *ACS Nano* **2020**, *14*, 8816.
[31] J. Wang, C. Fang, J. Ma, S. Wang, L. Jin, W. Li, D. Li, *ACS Nano* **2019**, *13*, 9473.
[32] Z. Guo, J. Li, R. Chen, T. He, *Prog. Quantum Electron.* **2022**, *82*, 100375.
[33] Y. Dang, X. Liu, Y. Sun, J. Song, W. Hu, X. Tao, *J. Phys. Chem. Lett.* **2020**, *11*, 1689.
[34] Y. Cao, N. Wang, H. Tian, J. Guo, Y. Wei, H. Chen, Y. Miao, W. Zou, K. Pan, Y. He, H. Cao, Y. Ke, M. Xu, Y. Wang, M. Yang, K. Du, Z. Fu, D. Kong, D. Dai, Y. Jin, G. Li, H. Li, Q. Peng, J. Wang, W. Huang, *Nature* **2018**, *562*, 249.
[35] Z. Ren, J. Yu, Z. Qin, J. Wang, J. Sun, C. C. S. Chan, S. Ding, K. Wang, R. Chen, K. S. Wong, X. Lu, W. J. Yin, W. C. H. Choy, *Adv. Mater.* **2021**, *33*, 2005570.
[36] S. Ma, Y. K. Jung, J. Ahn, J. Kyhm, J. Tan, H. Lee, G. Jang, C. U. Lee, A. Walsh, J. Moon, *Nat. Commun.* **2022**, *13*, 3259.
[37] J. Son, S. Ma, Y. K. Jung, J. Tan, G. Jang, H. Lee, C. U. Lee, J. Lee, S. Moon, W. Jeong, A. Walsh, J. Moon, *Nat. Commun.* **2023**, *14*, 3124.
[38] J. T. Lin, D. G. Chen, L. S. Yang, T. C. Lin, Y. H. Liu, Y. C. Chao, P. T. Chou, C. W. Chiu, *Angew. Chem., Int. Ed.* **2021**, *60*, 21434.
[39] M. K. Jana, R. Song, H. Liu, D. R. Khanal, S. M. Janke, R. Zhao, C. Liu, Z. Valy Vardeny, V. Blum, D. B. Mitzi, *Nat. Commun.* **2020**, *11*, 4699.
[40] Z. Wang, X. Wang, Z. Chen, Y. Liu, H. Xie, J. Xue, L. Mao, Y. Yan, H. Lu, *Angew. Chem., Int. Ed.* **2023**, *62*, 202215206.
[41] J. Huang, T. Lei, M. Siron, Y. Zhang, S. Yu, F. Seeler, A. Dehestani, L. N. Quan, K. Schierle-Arndt, P. Yang, *Nano Lett.* **2020**, *20*, 3734.
[42] H. Zhang, J. Yao, Y. Yang, H. Fu, *Chem. Mater.* **2021**, *33*, 2847.
[43] C. Wang, L. Ma, S. Wang, G. Zhao, *J. Phys. Chem. Lett.* **2021**, *12*, 12129.
[44] S. Ji, X. Yuan, W. Ji, H. Li, J. Zhao, H. Zhang, *J. Lumin.* **2022**, *245*, 118790.
[45] D. Cortecchia, W. Mróz, S. Neutzner, T. Borzda, G. Folpini, R. Brescia, A. Petrozza, *Chem* **2019**, *5*, 2146.
[46] R. Bakthavatsalam, A. Biswas, M. Chakali, P. R. Bangal, B. P. Kore, J. Kundu, *J. Phys. Chem. C* **2019**, *123*, 4739.
[47] S. Das, A. De, A. Samanta, *J. Phys. Chem. Lett.* **2020**, *11*, 1178.
[48] Y. Yamada, M. Hoyano, R. Akashi, K. Oto, Y. Kanemitsu, *J. Phys. Chem. Lett.* **2017**, *8*, 5798.
[49] B. Wang, C. Wang, Y. Chu, H. Zhang, M. Sun, H. Wang, S. Wang, G. Zhao, *J. Alloy Compd.* **2022**, *910*, 164892.
[50] M. Wang, X. Wang, B. Zhang, F. Li, H. Meng, S. Liu, Q. Zhao, *J. Mater. Chem. C* **2023**, *11*, 3206.
[51] X. Bai, H. Zhong, B. Chen, C. Chen, J. Han, R. Zeng, B. Zou, *J. Phys. Chem. C* **2018**, *122*, 3130.
[52] W. Kong, Z. Ye, Z. Qi, B. Zhang, M. Wang, A. Rahimi-Iman, H. Wu, *Phys. Chem. Chem. Phys.* **2015**, *17*, 16405.
[53] Y. Wei, C. Li, Y. Li, Z. Luo, X. Wu, Y. Liu, L. Zhang, X. He, W. Wang, Z. Quan, *Angew. Chem., Int. Ed.* **2022**, *61*, 202212685.
[54] D. Liang, H. Xiao, W. Cai, S. Lu, S. Zhao, Z. Zang, L. Xie, *Adv. Opt. Mater.* **2023**, *11*, 2202997.
[55] S. Wang, J. Ma, W. Li, J. Wang, H. Wang, H. Shen, J. Li, J. Wang, H. Luo, D. Li, *J. Phys. Chem. Lett.* **2019**, *10*, 2546.
[56] Y. Zhang, Y. Zhang, Y. Zhao, H. Jia, Z. Yang, B. Yin, Y. Wu, Y. Yi, C. Zhang, J. Yao, *J. Am. Chem. Soc.* **2023**, *145*, 12360.
[57] T. Chang, Y. Dai, Q. Wei, X. Xu, S. Cao, B. Zou, Q. Zhang, R. Zeng, *ACS Appl. Mater.* **2023**, *15*, 5487.
[58] T. Neumann, S. Feldmann, P. Moser, A. Delhomme, J. Zerhoch, T. van de Goor, S. Wang, M. Dyksik, T. Winkler, J. J. Finley, P. Plochocka, M.

S. Brandt, C. Faugeras, A. V. Stier, F. Deschler, *Nat. Commun.* **2021**, *12*, 3489.
[59] H. D. Ludowieg, M. Srebro-Hooper, J. Crassous, J. Autschbach, *ChemistryOpen* **2022**, *11*, 202200020.
[60] Z. Huang, B. P. Bloom, X. Ni, Z. N. Georgieva, M. Marciesky, E. Vetter, F. Liu, D. H. Waldeck, D. Sun, *ACS Nano* **2020**, *14*, 10370.
[61] Y. Liu, Y. Jiang, Z. Xu, L. Li, D. Zhang, W. Zheng, D. Liang, B. Zheng, H. Liu, X. Sun, C. Zhu, L. Lin, X. Zhu, H. Duan, Q. Yuan, X. Wang, S. Wang, D. Li, A. Pan, *Adv. Opt. Mater.* **2022**, *10*, 2200183.
[62] X. Lu, R. Hu, Y. Zhu, K. Song, W. Qin, *NPG Asia Mater* **2023**, *15*, 38.
[63] C. Zhang, X. Jiang, P. C. Sercel, H. Lu, M. C. Beard, S. McGill, D. Semenov, Z. V. Vardeny, *Adv. Opt. Mater.* **2023**, *11*, 2300436.
[64] R. Pan, K. Wang, Z. G. Yu, *Mater. Horiz.* **2022**, *9*, 740.
[65] Y. Dou, M. Wang, J. Zhang, H. Xu, B. Hu, *Adv. Funct. Mater.* **2020**, *30*, 2003476.
[66] A. Ishii, T. Miyasaka, *Sci. Adv.* **2020**, *6*, eabd3274.
[67] V. Morad, I. Cherniukh, L. Pöttschacher, Y. Shynkarenko, S. Yakunin, M. V. Kovalenko, *Chem. Mater.* **2019**, *31*, 10161.
[68] X.-H. Zhao, X. Hu, M.-E. Sun, X.-M. Luo, C. Zhang, G.-S. Chen, X.-Y. Dong, S.-Q. Zang, *J. Mater. Chem. C* **2022**, *10*, 3340.
[69] C. Ye, J. Jiang, S. Zou, W. Mi, Y. Xiao, *J. Am. Chem. Soc.* **2022**, *144*, 9707.
[70] X. H. Zhao, N. N. Li, J. Peng, J. Xu, P. Luo, X. Y. Dong, X. Hu, *Chem. Commun.* **2023**, *59*, 6881.